Radio Science, Volume 34, Number 4, Pages 841–858, July–August 1999

Simulation of radiometric and attenuation measurements along Earth-satellite links in the 10- to 50-GHz band through horizontally finite convective rain cells

Frank S. Marzano,[1] Ermanno Fionda,[2] and Piero Ciotti[1]

Abstract. An iterative solution is illustrated of the three-dimensional radiative transfer equation for a horizontally finite and vertically inhomogeneous precipitating cloud. The method is applied to modeling a convective rain cell of cylindrical shape, characterized by spherical raindrops having a negative-exponential drop size distribution. The realistic model also takes into account the presence of a cloud and an ice layer above the rain cell itself. The simulated brightness temperature, the mean radiative temperature, and the path attenuation are evaluated in a three-dimensional geometry from a surface observation point in order to simulate a ground-based station with a beacon receiver and a multichannel radiometer. Numerical results are shown to illustrate the potential of the proposed model for different sets of frequency channels, observation geometries, cloud sizes and types, and precipitation intensities. After generating a large data set by varying the relevant rain cell parameters, regression analysis is applied to derive a statistical estimation of the total path attenuation from surface rain rate and ground-based radiometric measurements together with the frequency scaling factors for cumuliform clouds in the 10- to 50-GHz band.

1. Introduction

Tropospheric attenuation due to precipitating clouds has a strong impact on terrestrial and satellite links in the microwave and millimeter-wave bands. For the usual elevation angles (5°–40°) and for carrier frequencies greater than 10 GHz, strong path attenuation has been measured in the case of cumulus clouds and convective precipitating storms [*Kozu et al*., 1988; *Watson and Hu*, 1992]. In the last 10 years, microwave radiometry has proved to be a valuable tool for estimating path attenuation and atmospheric parameters from both ground-based and satellite-borne microwave radiometers [*Westwater et al*., 1990; *Pierdicca et al*., 1996]. In particular, the potential of microwave radiometry in the telecommunications field is related to the possibility of evaluating the attenuation statistics for given frequency bands and geographical sites, without needing to set up expensive propagation experiments for the design of the link budget [*Schiavon et al*., 1993].

The estimate of path attenuation by microwave radiometry may be approached by using both experimental measurements and simulated data [*Crane*, 1985; *Fionda et al*., 1991]. The use of experimental measurements is limited by their scarcity, especially if referred to frequency bands higher than 20 GHz. Moreover, the determination of the fundamental parameters by best-fit of measurements makes questionable their application to other frequencies and locations. As a compromise, semiempirical methods have also been proposed by using both experimental data and theoretical considerations [*Capsoni et al*., 1987]. The modeling approach is generally more versatile since it does not require a large amount of reference data, even though it requires a thorough insight into the electromagnetic interaction between the microwave radiation and the scattering medium. The radiative transfer theory has so far been the most used approach to take into account the multiple scattering and the vertical inhomogeneity of the atmosphere [*Ishimaru and Cheung*, 1980; *Stamnes et al*., 1988; *Smith et al*., 1992]. However, the common hypothesis of a plane-parallel medium may not be adequate to describe the effect of horizontal finite dimensions of convective storms [*Kummerow and Weinman*, 1988]. This means that these models are not able to realistically address the case of cumuliform precipitating clouds and the extreme variability of rain within the antenna field of view [*Roberti et al*., 1994].

[1] Dipartimento di Ingegneria Elettrica, Università dell'Aquila, L'Aquila, Italy.
[2] Fondazione Ugo Bordoni, Rome, Italy.

Paper number 1999RS900030.
0048-6604/99/1999RS900030$11.00

In this paper we describe a numerical solution of the three-dimensional radiative transfer equation for a horizontally finite and vertically inhomogeneous precipitating cumulus. For simplicity we assume a cylindrical rain cell characterized by spherical raindrops having a negative-exponential drop size distribution, with cloud and ice layers above it. The simulated brightness temperature, the mean radiative temperature, and the path attenuation can be evaluated in a three-dimensional geometry along any direction from the surface observation point. Simulation results are also shown to illustrate the potential of the proposed model for different sets of channel frequency, observation geometry, cloud size and type, and precipitation intensity. Finally, regression analysis is applied to derive statistical estimation of the total path attenuation from surface rain rate and ground-based radiometric observations together with the attenuation frequency scaling factors in the 10- to 50-GHz band.

2. Three-Dimensional Radiative Transfer Model

A solution of the radiative transfer equation (RTE) in case of nonzero albedo is given by the iterative method by means of successive approximations [*Tsang et al*., 1985]. In this scheme the zeroth-order solution represents the case in which the multiple scattering is neglected. The nth-order solution is then obtained supposing the solution of order n-1 as a source of the multiple scattering term in the RTE, there being a correspondence between the order of scattering and the multiple scattering paths. In the next section an iterative method for RTE solution is presented for three-dimensional (3-D) absorbing and scattering media with finite geometry, thus removing the most common assumption of plane-parallel geometry.

2.1. Theoretical Framework

Let us suppose we have a statistically homogeneous scattering volume V and place the origin of the Cartesian reference system on its surface boundary S. This choice simplifies our notation but does not reduce the generality of our conclusions.

By referring to Figure 1a and expressing all the distance variables in optical units, we define τ as the observation vector and $\hat{\tau}$ as the unit vector along the propagation direction. Within the volume V the differential cylindrical volume dV, whose position is given by the source vector τ', identifies a differential solid angle $d\Omega$ along the propagation direction subtended by the cylinder differential base $d\Sigma$ so that the vertex of the $d\Omega$ cone is pointed by τ. The unit vector $\hat{\tau}'$ indicates directions other than the propagation ones $\hat{\tau}$ and defines the differential solid angle $d\Omega'$. Finally, the vector τ_i indicates the position on the surface S, where the incident radiation couples with the propagation direction $\hat{\tau}$, and τ is the optical distance along the propagation direction from the surface boundary S at τ_i.

By using the above notation, the radiative transfer equation describing the differential variations (per unit optical length) of the unpolarized spectral brightness temperature $T_B(\tau, \hat{\tau})$ at the location τ along the direction $\hat{\tau}$ can be written as

$$\frac{dT_B(\tau, \hat{\tau})}{d\tau} = -T_B(\tau, \hat{\tau}) + J(\tau, \hat{\tau}) \tag{1a}$$

where the so-called source function J is given by

$$J(\tau, \hat{\tau}) = \frac{w(\tau)}{4\pi} \int_{4\pi} p(\tau, \hat{\tau}, \hat{\tau}') T_B(\tau, \hat{\tau}')\, d\Omega' + [1 - w(\tau)]T(\tau) \tag{1b}$$

where w is the volumetric albedo, p is the scattering phase function (normalized to 1), and T is the physical temperature distribution within the volume. We will consider the integral form of (1a), that is,

$$T_B(\tau, \hat{\tau}) = T_B(\tau_i, \hat{\tau}) e^{-|\tau_i - \tau|} + \int_{\tau}^{\tau_i} J(\tau', \hat{\tau}) e^{-|\tau' - \tau|}\, d\tau' \tag{2}$$

where $T_B(\tau_i, \hat{\tau})$ is the radiation incident on the boundary surface at τ_i, coupled through the scattering phase function along the propagation direction [*Tsang et al*., 1985].

Since the source function J contains the unknown $T_B(\tau, \hat{\tau})$, equation (2) represents an integral equation whose solution is not trivial. In general, numerical and analytical approaches can be used to solve it under the assumption of a plane-parallel scattering medium, that is, in case of a one-dimensional (1-D) RTE. The most used method is the discretization of T_B directions both zenithally and azimuthally, for example, adopting the discrete-ordinate eigenvalue method [*Stamnes et al*., 1988; *Tsang et al*., 1985]. If a first-order zenithal and azimuthal expansion of T_B in Legendre and Fourier series, respectively, is accomplished (Eddington's approximation), an analytical

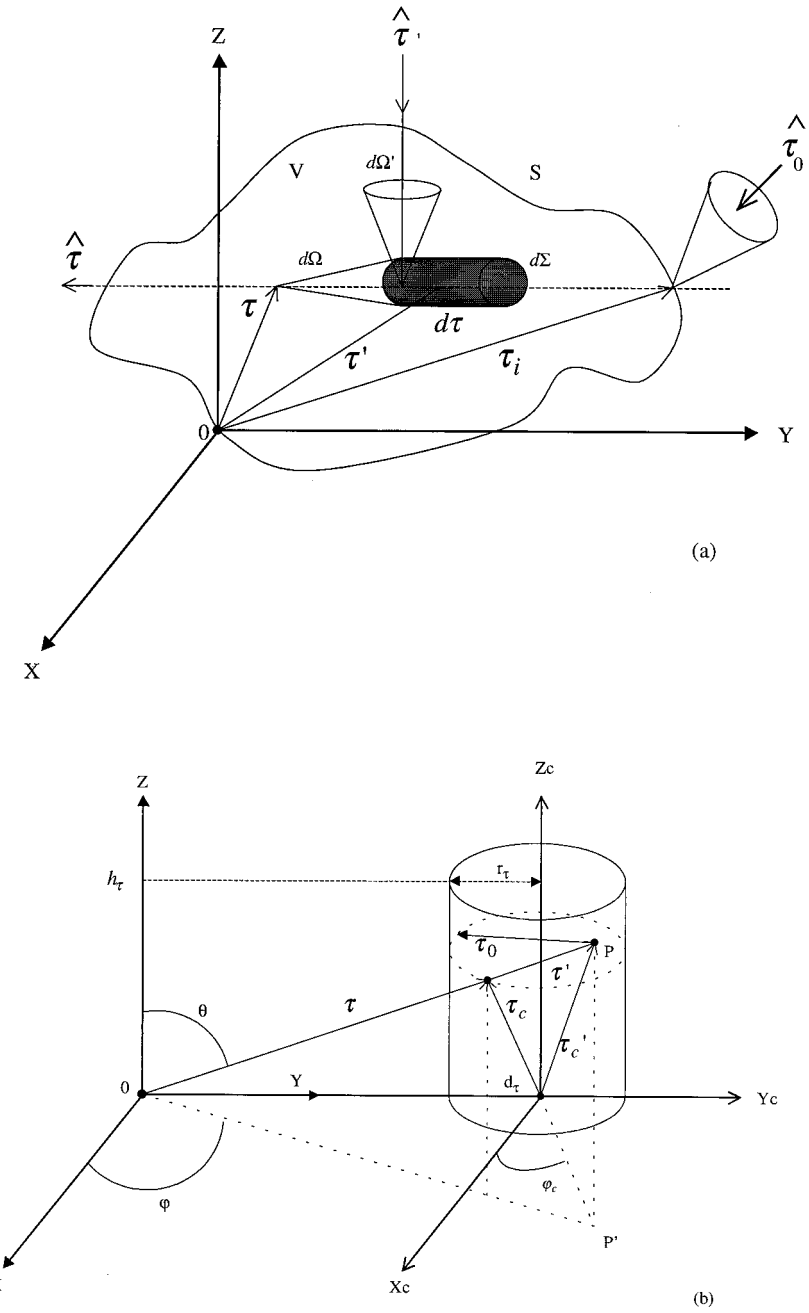

Figure 1. (a) Geometry for the general formulation of the radiative transfer equation (RTE) for scattering finite volumes. All the variables are supposed to be expressed in optical units. (b) Reference systems for the particular case of a finite circular cylinder.

solution of a 1-D RTE can be derived [*Wu and Weinman*, 1984; *Smith et al*., 1994]. The Eddington approximation has also been applied to three-dimensional (3-D) RTE problems having a simple volume geometry [*Kummerow and Weinman*, 1988]. For more general volume shapes the finite difference Monte Carlo method has proved to be a valuable technique to solve the RTE, even though requiring a large amount of computing time [*Roberti et al*., 1994].

Following the theoretical framework of *Brussaard*

[1985], here we want to illustrate a method to solve an RTE for 3-D scattering problems under the simplifying hypothesis of isotropic scattering within the volume, i.e., $p(\tau, \hat{\tau}, \hat{\tau}') = 1$. The validity of the latter assumption for atmospheric propagation will be discussed later. We also assume a constant volumetric albedo w and a constant physical temperature T within the volume V. The rationale of the method is to find a solution for the source function J by a recursive technique and then to use (2) to calculate the observed brightness temperature. In order to do this, it is convenient to define the angular average of T_B as

$$U(\tau) = \frac{1}{4\pi} \int_{4\pi} T_B(\tau, \hat{\tau}')\, d\Omega' \tag{3}$$

and to reexpress the integral form of the RTE in terms of $U(\tau)$, supposing for simplicity a null incident radiation (this hypothesis will be removed later on), that is,

$$U(\tau) = \int_V (1 - w)TH(|\tau - \tau'|)\, dV' + \int_V wU(\tau')H(|\tau - \tau'|)\, dV' \tag{4a}$$

where dV' is the differential (cylindrical) volume such that $dV' = d\Sigma' d\tau' = |\tau - \tau'|^2 d\tau' d\Omega'$ and the kernel function H is given by

$$H(|\tau - \tau'|) = \frac{e^{-|\tau - \tau'|}}{4\pi|\tau - \tau'|^2}. \tag{4b}$$

In order to solve (4a), a more compact form of $U(\tau)$ can be written by using the convolution operator $\otimes$ so that [*Brussaard*, 1985]

$$U(\tau) = (1 - w)T \otimes H(\tau) + wU(\tau) \otimes H(\tau) \tag{5a}$$

which can be easily Laplace transformed, obtaining

$$u(\mathbf{s}) = (1 - w)T\delta(\mathbf{s}) \left[\frac{h(\mathbf{s})}{1 - wh(\mathbf{s})}\right] = (1 - w)T\delta(\mathbf{s}) \sum_{n=0}^{\infty} w^n h(\mathbf{s})^{n+1} \tag{5b}$$

where $u(\mathbf{s})$ and $h(\mathbf{s})$ are the Laplace transforms of $U(\tau)$ and $H(\tau)$, respectively, with $\mathbf{s}$ being the transform vectorial variable and $\delta(\mathbf{s})$ being the Dirac function. By recognizing in the second member of (5b) the summation of a geometrical series in the Laplace domain, we obtain by antitransforming the third member of (5b) [*Brussaard*, 1985]

$$U(\tau) = (1 - w)T \otimes \sum_{n=0}^{\infty} w^n [H(\tau)]^{n+1} = \sum_{n=0}^{\infty} U_n(\tau) \tag{6a}$$

where U_n is the nth term of the average brightness temperature expansion. For (6) the following recursive relationships hold:

$$U_0(\tau) = (1 - w)T \otimes H(\tau) \qquad n = 0 \tag{6b}$$

$$U_n(\tau) = wU_{n-1}(\tau) \otimes H(\tau) \qquad n > 0. \tag{6c}$$

Thus, using (1b), the unknown source function J can also be expressed as a series expansion:

$$J(\tau) = (1 - w)T + wU(\tau) = \sum_{n=0}^{\infty} J_n(\tau) \tag{7a}$$

using the following recursive relationships:

$$J_0(\tau) = (1 - w)T \qquad n = 0 \tag{7b}$$

$$J_n(\tau) = wU_{n-1}(\tau) = wJ_{n-1}(\tau) \otimes H(\tau) \qquad n > 0. \tag{7c}$$

The series truncation at the Nth term gives [*Brussaard*, 1985]

$$J(\tau) = \sum_{n=0}^{N-2} J_n(\tau) + \frac{J_{N-1}(\tau)}{[1 - J_N(\tau)/J_{N-1}(\tau)]}. \tag{8}$$

The physical interpretation of (7a) is that each term $J_n(\tau)$ corresponds to the nth order of multiple scattering within the volume V.

In case of the presence of the incident radiation $T_B(\tau_i, \hat{\tau})$ on the surface S of the volume, it is easy to show that (7b) and (7c) must be replaced by the following recursive relationships:

$$J_0(\tau) = (1 - w)T \qquad n = 0 \tag{9a}$$

$$J_1(\tau) = w[J_0(\tau) \otimes H(\tau) + U(\tau, \tau_i)] \qquad n = 1 \tag{9b}$$

$$J_n(\tau) = wJ_{n-1}(\tau) \otimes H(\tau) \qquad n > 1 \tag{9c}$$

where

$$U(\tau, \tau_i) = \int_{4\pi} T_B(\tau_i, \hat{\tau}') e^{-|\tau - \tau_i|}\, d\Omega' = \int_S T_B(\tau_i, \hat{\tau}') H(|\tau_i - \tau|)\, dS' \tag{10}$$

where $U(\tau, \tau_i)$ is the irradiance over the boundary surface S, calculated at the input location τ_i.

2.2. Case of Cylindrical Finite Volume

The theory, illustrated so far, is valid for any volume geometry in 3-D space. For specific applications it is interesting to refer to some canonical problems, where the volume geometry can be easily described in a conventional reference system. Stratiform precipitation is generally modeled by horizontally infinite slabs so that the plane-parallel assumption may be applied [*Slobin*, 1982]. In case of atmospheric precipitation, convective rain cells can be idealized as finite volumes whose section and height may depend on the precipitation intensity itself [*Capsoni et al.*, 1987; *Mass*, 1987; *Kummerow and Weinman*, 1988].

In order to formally approach this problem, we will refer to the observation and volume geometry depicted in Figure 1b. The observation point (antenna site) is supposed to be in the origin of a spherical coordinates system (τ, θ, φ) at a distance d (d_τ in optical units) from the axis of the volume V, having a cylindrical form with radius r (r_τ in optical units) and height h (h_τ in optical units). The observation vector τ is chosen with its extreme on the cylinder surface, and, with respect to Figure 1a, τ becomes parallel to the source vector τ'. Within the finite cylinder, a cylindrical coordinate system (z_c, ρ_c, φ_c) is assumed so that if τ_c and τ_c' are the observation and source vectors with respect to the cylinder origin in $\tau = d_\tau$, $\theta = \pi/2$, $\varphi = \pi/2$, respectively, then holds: $\tau_c = \tau - d_\tau \hat{\mathbf{y}}$ and $\tau_c' = \tau' - d_\tau \hat{\mathbf{y}}$, with $\hat{\mathbf{y}}$ being the y-coordinate unit vector.

Let us rewrite the recursive relationship given in (9c) in the cylindrical coordinate system of Figure 1b, that is,

$$J_n(z_c, \rho_c, \varphi_c) = w \int_{V_c} J_{n-1}(z_c', \rho_c', \varphi_c') \cdot H(z_c, \rho_c, \varphi_c, z_c', \rho_c', \varphi_c')\, dV_c' \tag{11}$$

where V_c is the finite cylinder volume. A simplifying choice is to express (11), using a further spherical coordinate system $(\tau_P, \theta_P, \varphi_P)$ with origin in the source point $P(z_c, \rho_c, \varphi_c)$. If $\mu_P = \cos\theta_P$ and $\tau_0 = \tau_0(z_c, \rho_c, \varphi_c)$ is the optical distance between the generic source point P and a point on the cylinder surface, then we explicitly have in P

$$J_n(z_c, \rho_c, \varphi_c) = \frac{w}{2\pi} \int_0^{\tau_0} \int_{-1}^{+1} \int_0^{\pi} J_{n-1}(\tau_P', \mu_P', \varphi_P') e^{-\tau_P'} d\tau_P'\, d\mu_P'\, d\varphi_P'. \tag{12}$$

It is worth noting that the advantage in using (12) instead of (11) is that we can avoid the singularity due to the kernel function H.

The calculation of the triple integral in (12) can be carried out by discretizing the finite cylinder into subvolumes, using the circular symmetry around the vertical axis and the assumed homogeneity of the volume. In particular, in order to derive the first-order expansion J_1 we need to evaluate the following integral I_1:

$$I_1(z_c, \rho_c, \varphi_c) = \int_{V_c} H(|\tau - \tau'|)\, dV_c = \int_0^{\tau_0} \int_{-1}^{+1} \int_0^{\pi} \frac{e^{-\tau_P'}}{4\pi} d\tau_P'\, d\mu_P'\, d\varphi_P'. \tag{13}$$

Dividing the homogeneous cylinder into two parts with respect to its half height, if $\tilde{z}_c$ is the height symmetric to z_c with respect to the half-height plane, we can express

$$I_1(z_c, \rho_c, \varphi_c) = \bar{I}_1(z_c, \rho_c, \varphi_c) + \bar{I}_1(\tilde{z}_c, \rho_c, \varphi_c) \tag{14a}$$

where

$$\bar{I}_1(z_c, \rho_c, \varphi_c) = \int_0^{\tau_0} \int_{-1}^{0} \int_0^{\pi} \frac{e^{-\tau_P'}}{4\pi} d\tau_P'\, d\mu_P'\, d\varphi_P'. \tag{14b}$$

Thus, in case of incident radiation and noting that J_0 is constant (see equation (9a)), the first-order term of the source function, given in (9c), can be calculated by

$$J_1(z_c, \rho_c, \varphi_c) = wJ_0 I_1(z_c, \rho_c, \varphi_c) + wU(z_c, \rho_c, \varphi_c, z_{ci}, \rho_{ci}, \varphi_{ci}) \tag{15}$$

where $U(z_c, \rho_c, \varphi_c, z_{ci,}, \rho_{ci}, \varphi_{ci})$ is the incident average radiation on the surface border. It is easy to show that the latter term can be derived from

$$U(z_c, \rho_c, \varphi_c, z_{ci,}, \rho_{ci}, \varphi_{ci}) = U(z_{ci,}, \rho_{ci}, \varphi_{ci}) \cdot [1 - \bar{I}_1(z_c, \rho_c, \varphi_c) - \bar{I}_1(\tilde{z}_c, \rho_c, \varphi_c)] \tag{16a}$$

where

$$U(z_{ci}, \rho_{ci}, \varphi_{ci}) = \frac{1}{4\pi} \int_{-1}^{+1} \int_{0}^{\pi} T_B(z_{ci}, \rho_{ci}, \varphi_{ci}, \mu'_P, \varphi'_P)\, d\mu'_P\, d\varphi'_P. \quad (16b)$$

For higher-order terms the recursive relationships given in (9c) can be evaluated by

$$\begin{aligned} J_n(z_c, \rho_c, \varphi_c) &= w^n(1-w)T \\ &\cdot [\tilde{I}_n(z_c, \rho_c, \varphi_c) + \tilde{I}_n(\tilde{z}_c, \rho_c, \varphi_c)] \\ &+ w^n U(z_{ci,}, \rho_{ci}, \varphi_{ci}) \\ &\cdot [\tilde{I}_{n-1}(z_c, \rho_c, \varphi_c) + \tilde{I}_{n-1}(\tilde{z}_c, \rho_c, \varphi_{c-}) \\ &- \tilde{I}_n(z_c, \rho_c, \varphi_c) - \tilde{I}_n(\tilde{z}_c, \rho_c, \varphi_{c-})] \end{aligned} \quad (17a)$$

where

$$\tilde{I}_n(z_c, \rho_c, \varphi_c) = 1 \otimes H^n(z_c, \rho_c, \varphi_c). \quad (17b)$$

In conclusion, (9a), (15), and (17a) allow us to calculate the unknown source function J within the cylindrical volume V in case of incident radiation. Thus, by using (2), we can compute the observed brightness temperature $T_B(\tau, \theta, \varphi)$ for any direction (θ, φ) and position τ on the cylinder surface. In order to derive the brightness temperature $T_B(\tau = 0, \theta, \varphi)$ at the origin of the observation coordinate system of Figure 1b, the atmospheric attenuation and emission between the cylinder surface and the origin itself have to be taken into account.

In many applications it is useful to introduce the mean radiative temperature $T_{mr}(\tau, \theta, \varphi)$ of the scattering volume. Referring to Figure 1b, from (2) we can define

$$\begin{aligned} T_{mr}(\tau, \theta, \varphi) &\equiv \frac{\int_{\tau}^{\tau_i} J[\tau', \theta, \varphi] e^{-(\tau'-\tau)}\, d\tau'}{1 - e^{-(\tau_i - \tau)}} \\ &= \frac{T_B(\tau, \theta, \varphi) - T_B(\tau_i, \theta, \varphi) e^{-(\tau_i - \tau)}}{1 - e^{-(\tau_i - \tau)}} \end{aligned} \quad (18)$$

where τ_i is the optical distance along the propagation direction between the radiation incidence point on the cylinder surface and the observation point. For a partially scattering volume, we have $(1 - w)T \leq T_{mr} \leq T$, where the lower and upper limits correspond to the case of single scattering approximation (i.e., $J = J_0$ as in equation (9a)) and nonscattering medium (i.e., $w = 0$), respectively.

On the other hand, from brightness temperature measurements it is also possible to derive the total path attenuation $A(\tau, \theta, \varphi)$. Referring again to Figure 1b, from (18) we can define

$$\begin{aligned} A(\tau, \theta, \varphi) &\equiv 4.343(\tau_i - \tau) \\ &= 4.343 \ln \left[\frac{T_{mr}(\tau, \theta, \varphi) - T_B(\tau_i, \theta, \varphi)}{T_{mr}(\tau, \theta, \varphi) - T_B(\tau, \theta, \varphi)} \right] \end{aligned} \quad (19)$$

where A is expressed in decibels. Note that the attenuation depends on the zenithal and azimuthal angles, i.e., on the geometry of the observation in the 3-D space.

2.3. Convective Rain Cell Characterization

Convective precipitation is usually attributed to cumulonimbi whose main features are to be horizontally finite (some kilometers) and strongly vertically extended (up to the tropopause) [*Houze*, 1981; *Smith et al.*, 1992]. Cylindrical shape for convective rainfall is a common idealization, and this is the reason why we have specialized our 3-D model for finite circular cylinders. Because of their large vertical extension which goes across the zero-degree isotherm, cumulonimbi present liquid and ice phase in a precipitating and nonprecipitating form [*Wu and Weinman*, 1984; *Basili et al.*, 1995]. However, as a first step, in order to analyze the impact of the finite horizontal extension of the rain cell on the simulated observables, we have dealt with a simple reference case.

The reference case consists of a cylinder of radius r and height h, having a distance d from the ground-based observation point at $\tau = 0$. The cylinder and the space outside have been supposed to be filled with humid air whose atmospheric profiles have been derived from the U.S. Standard Atmosphere (1962) [*Ulaby et al.*, 1982], choosing a ground surface temperature T_s of 21°C and a relative humidity of 80%. The cylinder radius r has been fixed at 1 km, while its height h has been fixed equal to the zero-degree isotherm altitude, i.e., about 3 km if the thermal gradient is −6.5 K/km; the distance d has been set to 3 km so that the observation is outside the cylinder. The rain cell was assumed to be filled by spherical raindrops, having a Marshall-Palmer particle size distribution (PSD) as a function of the surface rain rate [*Olsen et al.*, 1978] with a drop temperature equal to the average of the rain cell bottom and top surface temperatures (i.e., 10.5°C). The microwave spectral absorption of gaseous constituents has been computed by the Liebe model [*Liebe et al.*, 1989], while

the extinction coefficient and scattering phase function of spherical raindrops have been derived from the Mie theory [*Wiscombe*, 1978] and by integrating over the given PSD. The emissivity model of the ground surface (lower boundary condition) has been chosen of Lambertian type, as a function of surface humidity [*Smith and Mugnai*, 1988]. On the surface of the cylinder a cosmic background radiation was assumed to be incident.

Aiming at more realistic simulations, we have also adopted different schemes as modifications of the reference case. We have assumed a horizontally infinite layer of spherical cloud particles of thickness determined by the distance between the +5°C and −5°C isothermal (about 1.5 km with standard thermal gradient) so that liquid and supercooled (above the zero thermal) droplets have been considered. The liquid water content of the cloud layer has been set equal to 1 g/m^3 [*Ulaby et al*., 1982], and its absorption has been derived from a relation given by *Slobin* [1982]; also, cloud content values of 0.5 g/m^3 have been considered. Above the cloud droplets a layer of equivalent-spherical ice particles having a thickness determined by the distance between the −5°C and −20°C isothermal (about 2.3 km with standard thermal gradient) has been added. A Sekhon-Srivastava PSD has been used for ice particles in order to compute extinction and albedo from the Mie theory [*Gasiewskii*, 1993]. Multiple scattering within the cloud and ice layers has been neglected for simplicity. In conclusion, the realistic case of a convective cloud consists of three parts: a cylindrically shaped rain cell, a nonprecipitating cloud layer, and an ice-crystal layer.

The cylindrical rain cell properties have been further varied in order to extend the sensitivity studies. A parametric form of the cylinder radius r has been adopted in order to simulate the reasonable decrease of rain cell horizontal dimension with the increase of the surface rain rate R. Several models are available in the literature [*Misme and Waldteufel*, 1980; *Mass*, 1987; *Capsoni et al*., 1987]. Since we were interested in a deterministic relation between r and R for a cylindrical rain cell, we adopted the following formula given by *Misme and Waldteufel* [1980]:

$$r = 1.1 \left(\frac{R}{100} \right)^{-0.4} \tag{20}$$

where r is in km and R is in mm/h. Finally, we have also changed in other cases the raindrop PSD, selecting the Joss one for thunderstorms [*Olsen et al*., 1978].

Let us finally consider some aspects of the solution method illustrated in the previous section. The iterative solution given in equations (9) has been derived under the restrictive assumption of isotropic scattering. This means that the scattering phase function is unitary, that is, its volumetric asymmetry factor g is zero [*Mugnai and Smith*, 1988; *Gasiewskii*, 1993]. Thus it is interesting to analyze in our application to convective rain cells the limits this condition imposes on the simulation parameters in the 10- to 50-GHz band, which we are interested in.

Figures 2a and 2b show the volumetric albedo w and asymmetry factor g at 13.0, 23.8, 31.6, and 50.2 GHz as a function of the surface rain rate R for a polydispersion of raindrops with a Marshall-Palmer PSD. For R up 75 mm/h the albedo is always less than 0.5 and increases monotonically due to the increase of scattering. Correspondingly, the asymmetry remains between −0.10 at 13.0 GHz, meaning that the backward scattering is dominant, and 0.15 at 50.2 GHz, where the forward scattering is the prevailing effect. For the intermediate frequencies at 23.8 and 31.6 GHz it is between −0.05 and 0.05. Thus we can conclude that for R less than 75 mm/h and in the 10- to 50-GHz frequency band the error due to the isotropic scattering assumption is, on average, less than 10%.

To compute the source function J through (15) and (17), the cylindrical volume has been divided into subvolumes, determined by the interception of concentric cylindrical surfaces with horizontal parallel planes. In particular, the diameter has been subdivided into 10 intervals and the height has been divided into 20 intervals. For media with $w < 0.6$, which is the rain cell case, it has been verified that a cutoff number N of the series expansion of J, given in (7), equal to 4 is sufficient to ensure the series convergence. After computing J within each subvolume, the integral of (2) (or equation (18)) has been computed through a Gauss-Legendre quadrature by selecting the subvolumes intercepted by the propagation direction line.

3. Simulation Results

The numerical simulations have been carried out at various frequencies in the 10- to 50-GHz band, mainly considering the operational ground-based microwave radiometers at 13.0, 23.8, 31.6, and 50.2 GHz [*Schiavon et al*., 1993] and current experimental satellite links, as the Italsat beacons at 18.7, 39.6, and 49.5

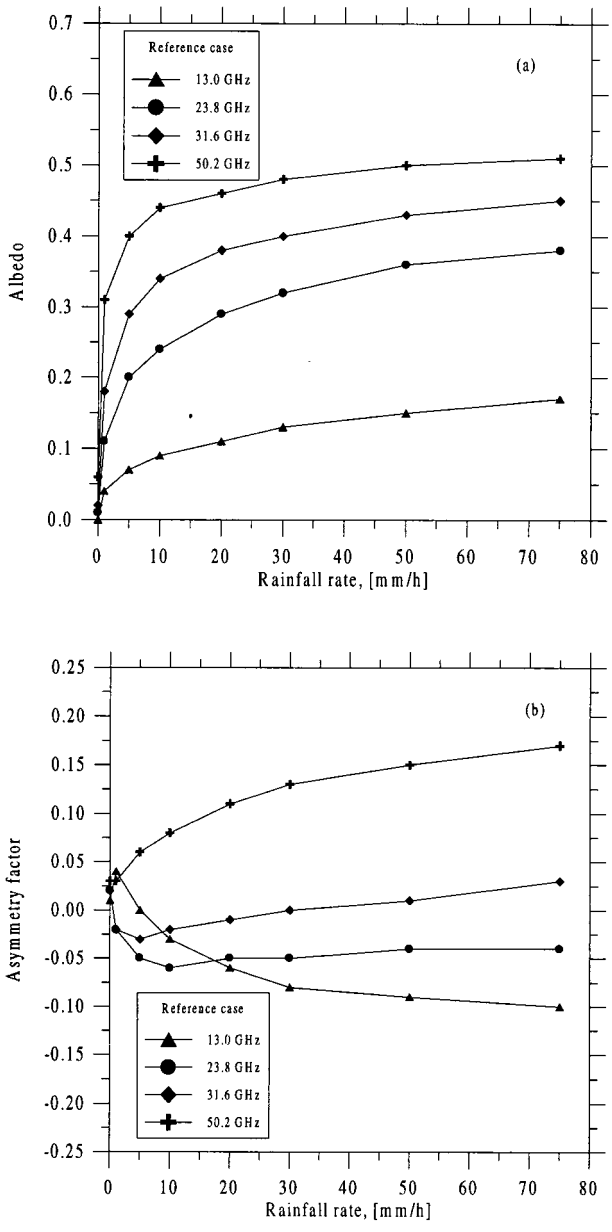

Figure 2. (a) Volumetric albedo and (b) asymmetry factor at 13.0, 23.8, 31.6, and 50.2 GHz as a function of the surface rain rate for a polydispersion of raindrops with a Marshall-Palmer particle size distribution (PSD) in the reference case.

GHz [*De Angelis et al.*, 1994]. In any case, we have supposed ground-based radiometeric and attenuation measurements, even though the solution method illustrated in section 2.1 could be applied also to spaceborne observations. We have analyzed several geometries of observation, varying the azimuthal and elevation angles, and the impact of the geometrical and microphysical properties of the convective rain cell. A comparison with a plane-parallel rain cell simulation has been also considered.

3.1. Impact of Observation Parameters

Let us start by considering the reference case as described in section 2.3, referring to Figure 1b. Figures 3a and 3b show the simulated brightness temperature T_B and mean radiative temperature T_{mr} at 13.0, 23.8, 31.6, and 50.2 GHz against rainfall rate R for a 20° elevation angle and 90° azimuthal angle (i.e., $\theta = 70°$ and $\varphi = 90°$).

For a given value of R, in Figure 3a the effect of emission and multiple scattering due to the raindrops increases as the channel frequency increases. Note that the value of R, for which T_B saturates, is inversely related to frequency. The simulation results show also distinct T_B initial values for each frequency, corresponding to a rainfall rate value of 0.01 mm/h, due to the different frequency-channel sensitivity to gaseous and raindrop emission. Moreover, up to 5 mm/h, T_B values at 31.6 GHz are lower than values at 23.8 GHz, due to water vapor emission.

The mean radiative temperature T_{mr} of the rain cell itself has been calculated using (18), which explains the behavior shown in Figure 3b. As R increases, the T_{mr} generally decreases following the decrease of the rain cell transmittance (which is associated with an increase of the albedo). However, as the precipitation becomes intense and at frequency greater than 30 GHz, there appears a minimum after which T_{mr} tends to increase with R. This can be explained by considering that as the albedo increases, the additive contribution of multiple scattering to total radiation becomes dominant with respect to the single-scattering decreasing effect.

Figure 4a shows the simulated total path attenuation A at 13.0, 23.8, 31.6, and 50.2 GHz, derived from (19), against rainfall rate R for a 20° elevation angle and 90° azimuthal angle. It is interesting to compare what total path attenuation we would expect if instead of using the simulated T_{mr} plotted in Figure 3b, which takes into account the multiple scattering effects, a fixed value were used. Elsewhere, such an attenuation has been called "apparent" total path attenuation [*Ishimaru and Cheung*, 1980].

Figure 4b shows the same as for Figure 4a, but for the apparent total path attenuation. The curves, indicated by solid lines, refer to a value equal to the physical rain cell temperature, that is, $T_{mr} = 283.5$ K

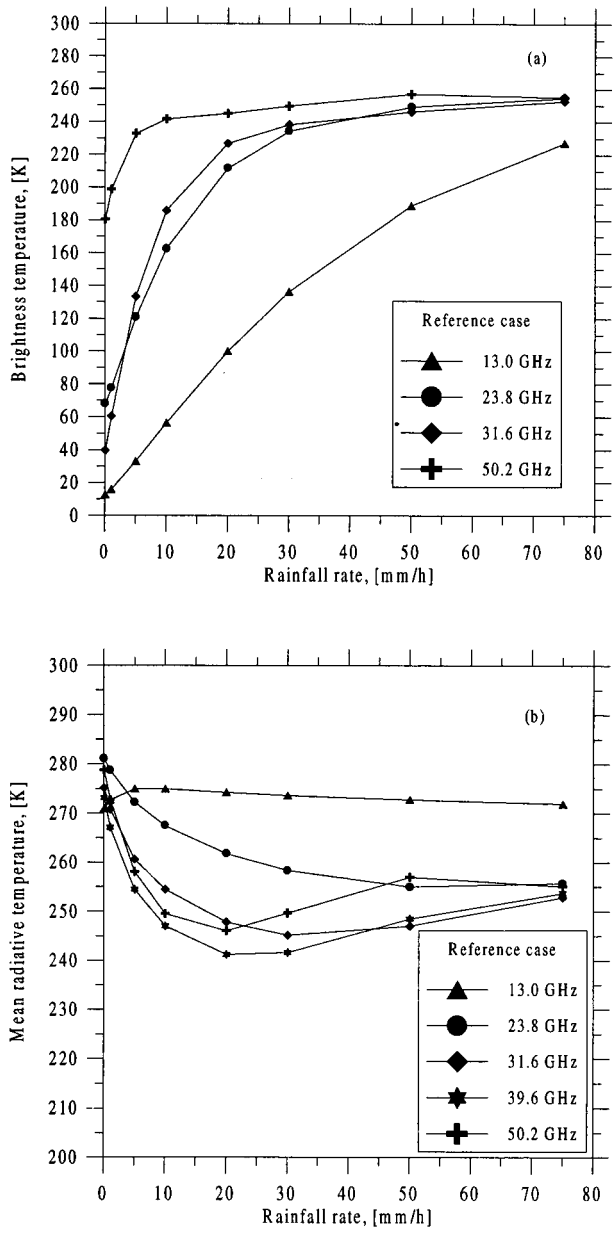

Figure 3. (a) Simulated brightness temperature and (b) mean radiative temperature at 13.0, 23.8, 31.6, and 50.2 GHz against rainfall rate R for a 20° elevation angle and 90° azimuthal angle in the reference case.

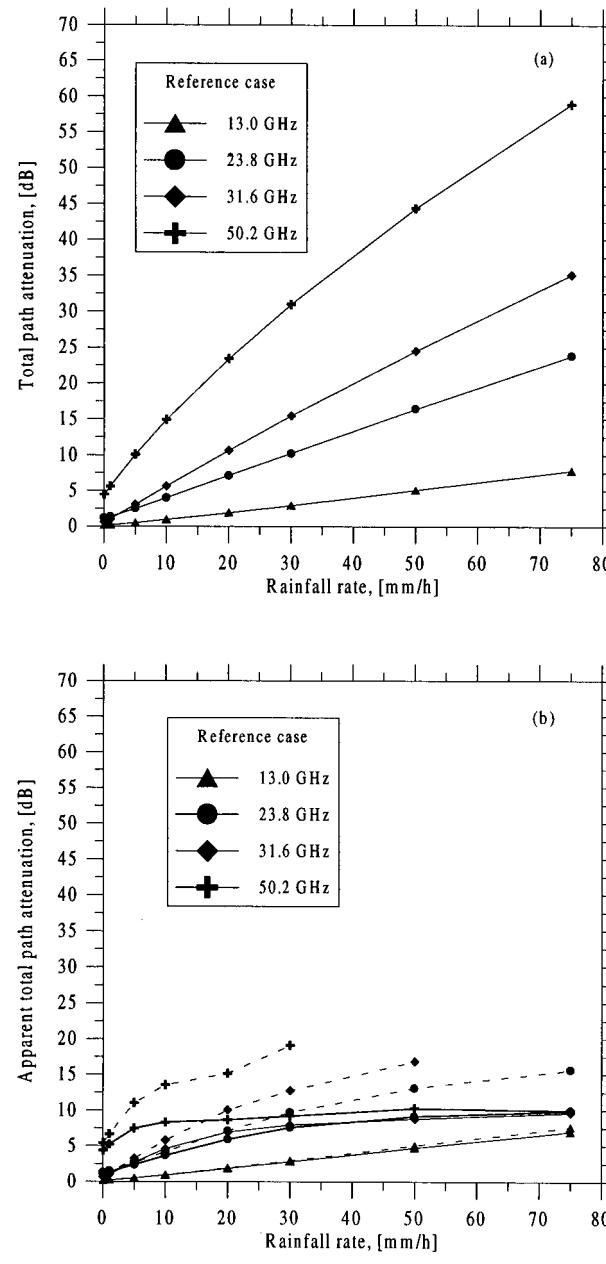

Figure 4. (a) Simulated total path attenuation and (b) "apparent" total path attenuation at 13.0, 23.8, 31.6, and 50.2 GHz against rainfall rate for a 20° elevation angle and 90° azimuthal angle in the reference case. In Figure 4b the curves, indicated by solid lines, refer to T_{mr} = 283.5 K (equal to the physical rain cell temperature) at any frequency and rainfall rate, while the dashed lines are derived by choosing a frequency-dependent T_{mr} value equal to 273.7, 261.8, 251.4, and 252.6 K at 13.0, 23.8, 31.6, and 50.2 GHz, respectively (attenuation values for $R > 50$ *mm/h at* 31.6 *and for* $R > 30$ mm/h at 50.2 GHz are not shown because $T_{mr} < T_B$ and equation (19) is undefined).

at any frequency and rainfall rate. The dashed lines in the same plot are derived by choosing a T_{mr} value variable with frequency, i.e., equal to 273.4, 261.8, 251.4, and 252.6 K at 13.0, 23.8, 31.6, and 50.2 GHz, respectively. These T_{mr} values are obtained from Figure 4a by averaging T_{mr} for $R > 5$ mm/h at each

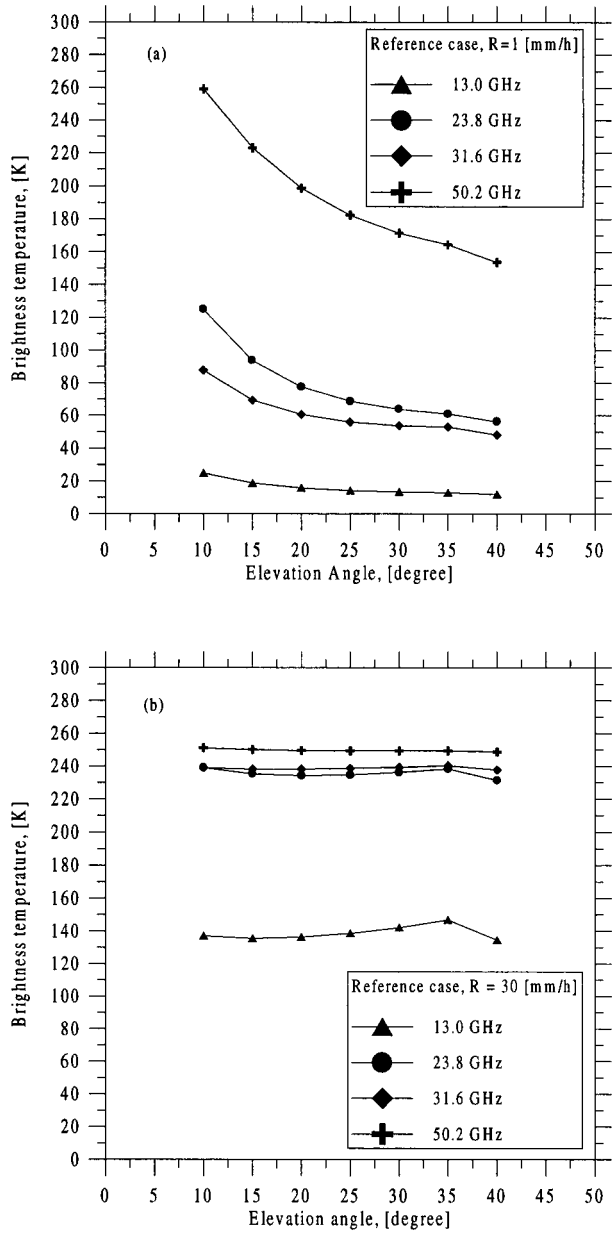

Figure 5. Simulated brightness temperature at 13.0, 23.8, 31.6, and 50.2 GHz against the elevation angle for rainfall rate of (a) $R = 1$ mm/h and (b) $R = 30$ mm/h for a 90° azimuthal angle in the reference case.

frequency; note that attenuation values for $R > 50$ mm/h at 31.6 GHz and $R > 30$ mm/h at 50.2 GHz are not shown because $T_{mr} < T_B$ and (19) becomes undefined.

From Figure 4b it is noted a significant underestimation of the "true" attenuation when using $T_{mr} =$ 283.5 K for frequencies greater than 13.0 GHz, while a better agreement is obtained when selecting a more appropriate frequency-dependent T_{mr} value. The difference between the true and apparent attenuation is again due to the multiple scattering process, which becomes dominant for rain intensities higher than 10 mm/h.

The impact of varying the elevation angle is illustrated in Figures 5a and 5b, which show the simulated brightness temperature T_B at 13.0, 23.8, 31.6, and 50.2 GHz against the elevation angle for rainfall rate $R = 1$ mm/h and $R = 30$ mm/h, respectively, again for a 90° azimuthal angle. In the absence of multiple scattering for $R \leq 1$ mm/h the simulation exhibits a monotonic decrease of T_B with the elevation angle. Conversely, in Figure 5b the simulation shows maximum values at θ equal to 35°, associated with the largest path length through the 3-D rain cell volume. Note that this effect cannot be derived from a 1-D RTE simulation [*Ishimaru and Cheung*, 1980].

Figure 6 shows the simulated brightness temperature T_B at 13.0, 23.8, 31.6, and 50.2 GHz against rainfall rate R for a 20° elevation angle and two values of the azimuthal angle, 90° and 75°. At any frequency the T_B values for $\varphi = 75°$ are lower than those at $\varphi = 90°$, a fact mainly dependent on the shorter optical path length through the 3-D rain cell associated with the received radiation in the case of $\varphi = 75°$.

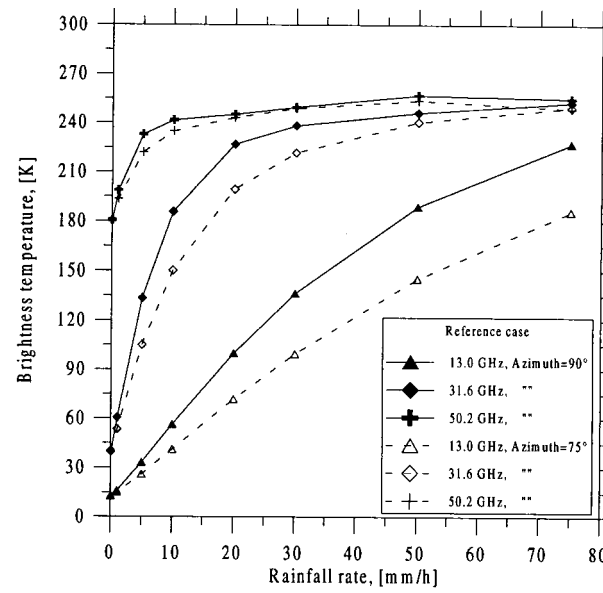

Figure 6. Simulated brightness temperatures at 13.0, 23.8, 31.6, and 50.2 GHz against rainfall rate R for a 20° elevation angle and two values (90° and 75°) of the azimuthal angle in the reference case.

3.2. Impact of Rain Cell Properties and Geometry

The choice of the PSD strongly affects the extinction of the raindrop polydispersion and thus the simulated brightness temperature. Actually, rain PSD varies with the geographic region and seasonal period, and even within the same precipitation event in time and space. Considering again the geometry of the reference case, Figures 7a and 7b show the volumetric albedo and attenuation (in decibels) at 13.0 and 50.2 GHz against rainfall rate, using the Marshall-Palmer (MP) PSD and Joss-thunderstorm (J–T) PSD [*Olsen et al.*, 1978], for a 20° elevation angle and 90° azimuthal angle, while Figure 8 shows the simulated brightness temperature at 13.0 and 50.2 GHz against the rainfall rate.

The behaviors in the previous figures can be explained if it is noticed that on one hand, the J–T PSD prescribes less small drops and more big drops than MP and, on the other hand, the J–T PSD is characterized by a much lower number of particles than MP PSD for the same rain rate. Thus the albedo and the optical thickness of the J–T distribution are higher and lower, respectively, than those of the MP one so that the corresponding T_B and total path attenuation A are smaller than the ones computed using the MP PSD.

The impact of having a variable rain cell radius, parameterized as in (20), is shown in Figure 9, where the simulated brightness temperatures at 13.0, 31.6, and 50.2 GHz against the rainfall rate are shown for a variable and 1-km fixed rain cell radius, considering the configuration of the reference case with a 20° elevation angle and 90° azimuthal angle. Equation (20) provides values of the rain cell radius ranging from 1.23 km for $R = 75$ mm/h to 43 km at $R = 0.01$ mm/h. Up to rainfall rates of 125 mm/h the simulated T_B with variable radius are greater than the values obtained with a constant radius of 1 km due to larger rainfall volumes. Conversely, for rain intensities higher than 125 mm/h, the T_B is lower since the cylinder radius becomes less than 1 km.

Finally, a realistic convective cloud with rain, cloud, and ice structures, as described in section 2.3, is considered in Figure 10, considering the simulation parameters of the reference case for the cylindrical rain cell for a 20° elevation angle and 90° azimuthal angle.

Figure 10a shows the simulated T_B at 13.0, 31.6, and 50.2 GHz due to the rain cell plus the droplet layer, as a function of the rainfall rate. As expected, when adding the cloud layer having a liquid content of 1 g/m^3 above the rain cylinder, the T_B further increases and the difference is larger for optically thin rain cells and high frequencies. However, the cloud effect is relevant up to values of rain rate, depending

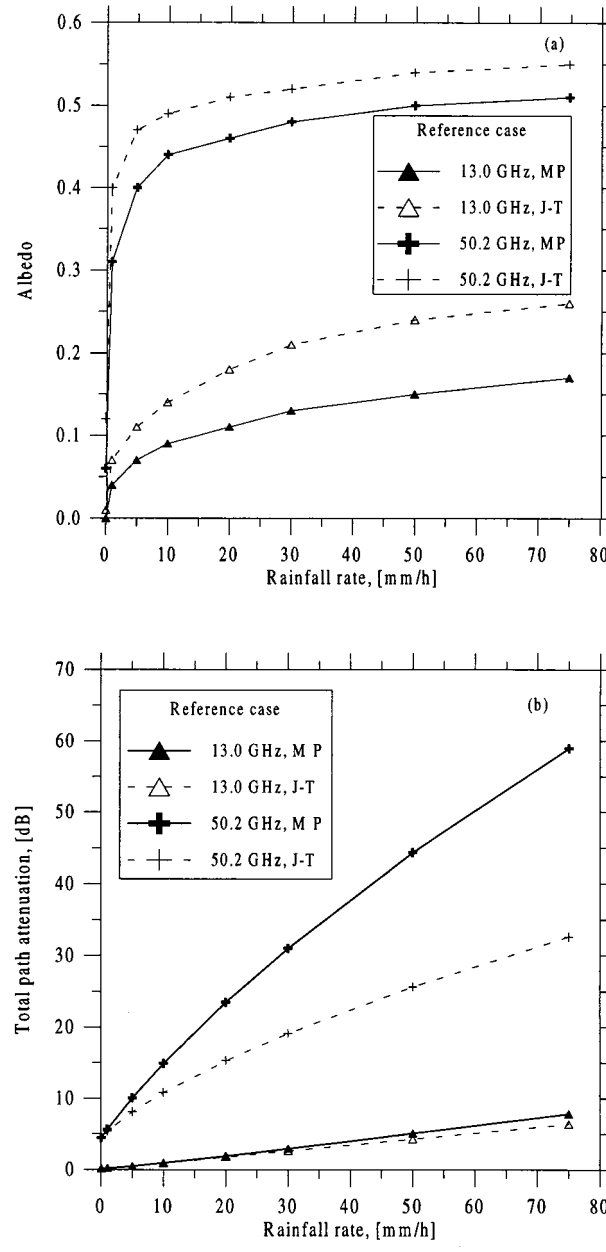

Figure 7. (a) Volumetric albedo and (b) total path attenuation at 13.0 and 50.2 GHz against rainfall rate, using the Marshall-Palmer (MP) PSD and Joss-thunderstorm (J–T) PSD, for a 20° elevation angle and 90° azimuthal angle in the reference case.

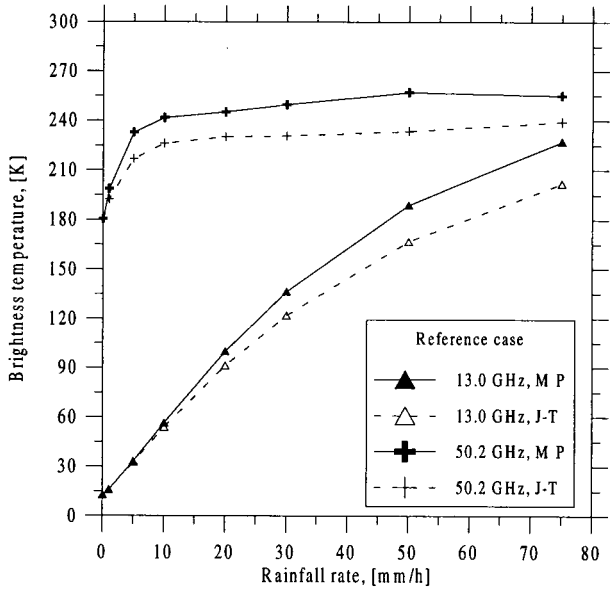

Figure 8. Simulated brightness temperature at 13.0 and 50.2 GHz against the rainfall rate, using the Marshall-Palmer PSD and Joss-thunderstorm PSD, for a 20° elevation angle and 90° azimuthal angle in the reference case.

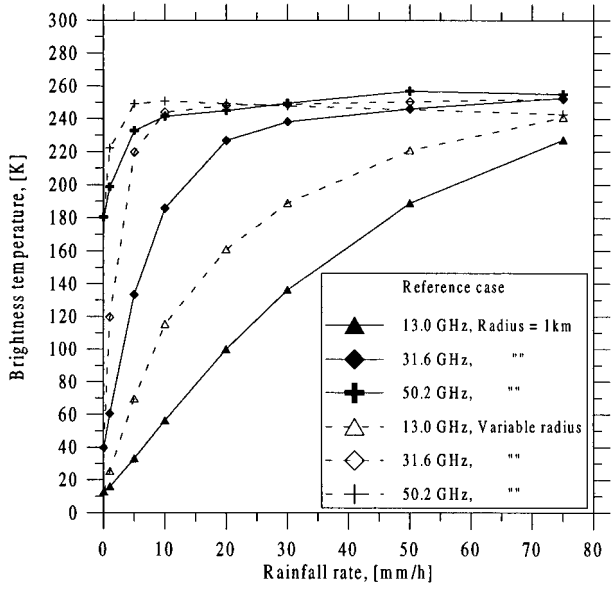

Figure 9. Simulated brightness temperature at 13.0, 31.6, and 50.2 GHz against the rainfall rate for a variable rain cell radius and 1-km fixed rain cell radius, for a 20° elevation angle and 90° azimuthal angle in the reference case.

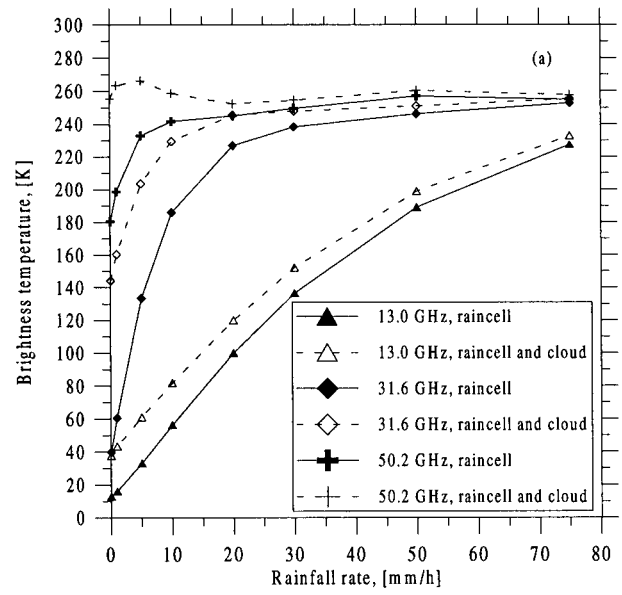

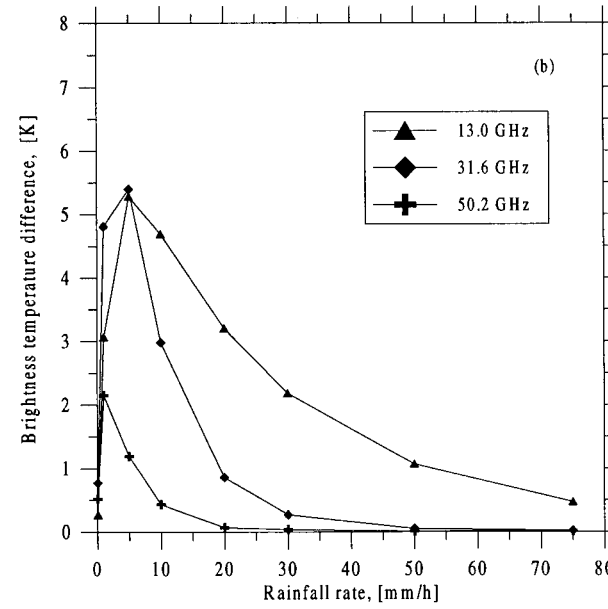

Figure 10. (a) Simulated brightness temperatures at 13.0, 31.6, and 50.2 GHz due to the rain cell plus the droplet layer and (b) difference between the simulated T_B due to the rain cell plus the droplet layer and the ice layer and to the rain cell plus the droplet layer only, as a function of the rainfall rate for a 20° elevation angle, a 90° azimuthal angle, and a 3-km distance from the cylindrical rain cell axis.

on frequency, beyond which the rain cell emission and scattering completely mask the cloud contribution.

Figure 10b shows the difference between the simulated T_B due to the addition of an ice layer to the rain cell plus the droplet structure considered for Figure 10a. In this case the difference shows a maximum value at 5 mm/h, after which it decreases as the rain rate and frequency increase. The maximum in the T_B difference is explained by considering the partially scattered emission of ice, which is relatively low and is washed out by rain and cloud extinction for R greater than 10 mm/h.

For brevity we do not show the results obtained by varying the surface temperature T_s and consequently reducing ($T_s < 21$°C for winter conditions) or increasing ($T_s > 21$°C for summer conditions) the vertical extension of the storm structures, due to the parameterization of the rain cell top height, as described in section 2.3. Apart from geometry the volumetric extinction and scattering of hydrometeors also depend on temperature. In general, brightness temperatures and total attenuations increase in summer conditions and decrease in winter conditions with respect to the average situation of the reference case.

3.3. Comparison With One-Dimensional Slab Results

In order to make this comparison we consider again the reference case for observations at 20° elevation angle and 90° azimuthal angle. As a solution of the 1-D RTE, we have considered the Eddington approximation, which also enables the evaluation of nonisotropic scattering for T_B computations [*Wu and Weinman*, 1984; *Smith et al.*, 1994]. As a result, we have found that within the rain rate and frequency ranges considered in this work, the effect of setting the asymmetry factor to zero (i.e., isotropic scattering) gives rise to errors for downwelling T_B due to homogeneous rain slabs less than 1 K.

Figures 11a and 11b show simulated T_B at 13 and 31.6 GHz, respectively, computed from the 3-D RTE algorithm, and the corresponding T_B derived from a slab of 3 km height with the same raindrop temperature and the same rain extinction and albedo of the 3-D case. The values for the 1-D case are higher than 3-D corresponding ones, and this difference increases as R increases. The T_B overestimation of 1-D simulations is mainly due to the higher optical thickness and multiple scattering contribution of the rain slab with respect to the cylindrical rain cell.

In order to explore the possibility of fitting the 1-D

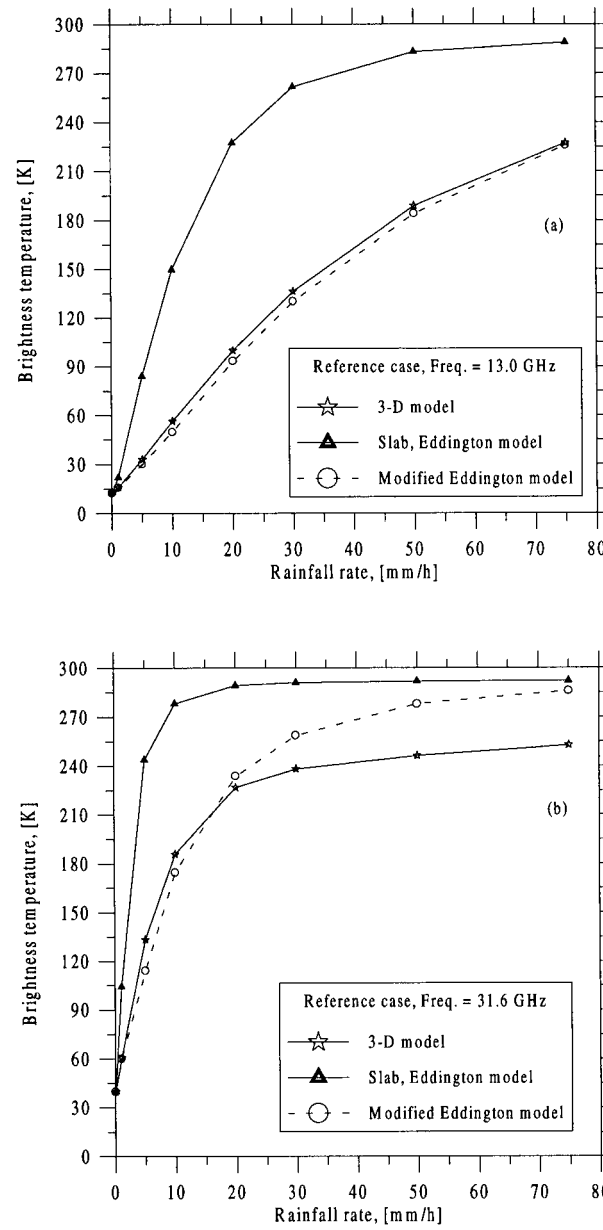

Figure 11. Simulated brightness temperature against the rainfall rate at (a) 13.0 GHz and (b) 31.6 GHz, computed by means of the 3-D RTE algorithm and 1-D RTE algorithm (consisting of a slab of 3 km height with the same raindrop temperature and the same rain extinction of 3-D case). Dashed lines indicate the results obtained by using the modified 1-D RTE algorithm with a slab of height equal to h_{eq} (see equation (21)).

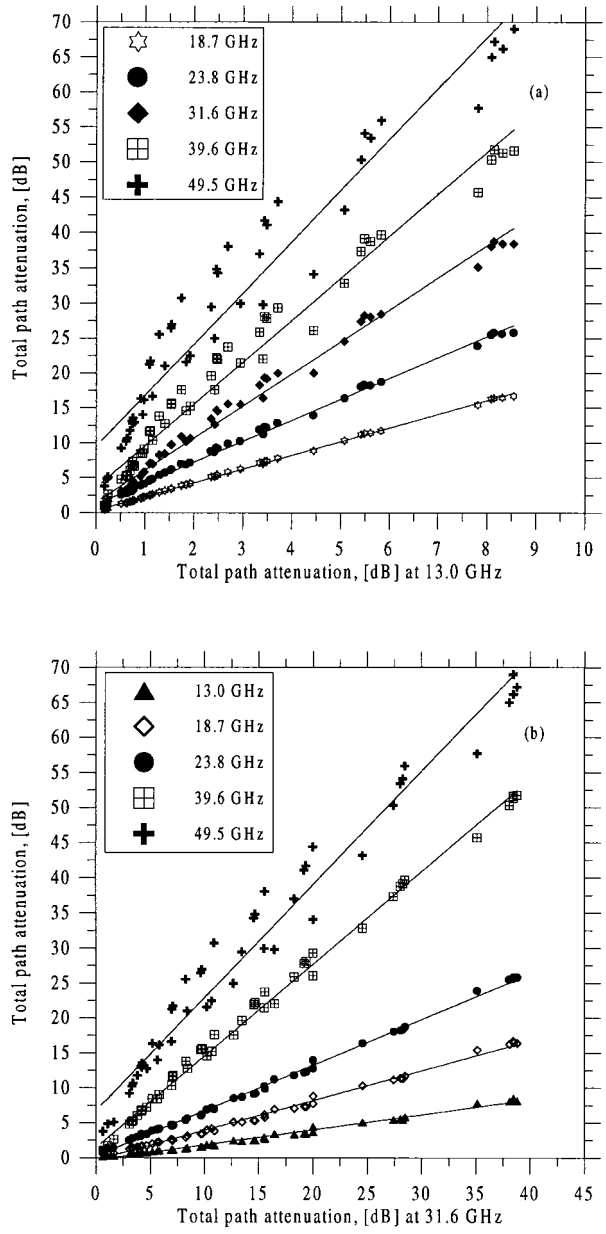

Figure 12. (a) Total path attenuation at 18.7, 23.8, 31.6, 39.6, and 49.5 GHz as a function of the total path attenuation at 13 GHz and (b) total path attenuation at 13.0, 18.7, 23.8, 39.6, and 49.5 GHz as a function of the total path attenuation at 31.6 GHz, using all the simulated data set for a 20° elevation angle. Linear best-fittings are also shown.

slab simulations to the 3-D results, we have defined an equivalent height h_{eq} of the slab as follows:

$$h_{eq}(\theta, \varphi; R, f) = \frac{\tau_{3D}}{\tau_{1D}} h \tag{21}$$

where τ_{3D} and τ_{1D} are the optical thickness computed for a 3-D cylinder and 1-D slab, respectively, and h is the cylinder height. It is clear that h_{eq} depends on rain rate R, frequency f, and also on the observation geometry; moreover, for $R = 0$ mm/h, we have $h_{eq} = h$ since the optical thickness in both the 1-D and 3-D cases is due only to the gaseous absorption, while for higher rain rate values it always results in $h_{eq} < h$ for observations outside the rain cell. The impact of using h_{eq} within 1-D simulations is shown in Figures 11a and 11b by dashed lines. The agreement between the 3-D T_B and the corresponding 1-D values is quite good at 13.0 GHz for any rain rate value, while at 31.6 GHz the agreement is satisfactory only for rain rates less than 20 mm/h. This means that under the approximation of isotropic scattering, 3-D effects on T_B can be effectively approximated by a modified 1-D RTE model of the convective rain cell only for cases where the albedo is less than about 0.15 where the multiple scattering contribution is quite limited. From another point of view, the 3-D geometry causes electromagnetic radiation to go outward from the cylinder and to be lost by the ground-based receiving antenna [*Roberti et al*., 1994]. In the limiting case of a cylinder with an infinite radius, the 3-D results tend to coincide with the 1-D slab ones for any albedo.

4. Attenuation Prediction in the 10- to 50-GHz Band

The ensemble of numerical simulations carried out varying all the simulation parameters has allowed us to construct a fairly large data set of total path attenuations and downwelling brightness temperatures due to finite convective rain cells. Note that the data set basically contains results for observations outside the rain cell with an elevation angle of 20°, also considering the presence of both gaseous and cloud absorption. In the following equations involving T_B and A we have indicated explicitly only the dependence on the channel frequency with respect to the more general expressions given in (18) and (19).

4.1. Attenuation Frequency Scaling

Figure 12a shows the total path attenuation at 18.7, 23.8, 31.6, 39.6, and 49.5 GHz as a function of the total path attenuation at 13.0 GHz using the whole simulated data set, while Figure 12b shows the same at 13.0, 18.7, 23.8, 39.6, and 49.5 GHz as a function of the total path attenuation at 31.6 GHz. In these

figures, solid lines represent the linear best-fit curve at each frequency.

As already noted, the total path attenuation strongly increases with frequency. Besides, a linear frequency scaling technique seems to be suitable for propagation purposes in the 10- to 50-GHz band. Thus statistical relationships to estimate the total path attenuation A (in decibels) from corresponding values, known at other frequencies, can be expressed in the following way:

$$A(f_j) = a_0 + a_1 A(f_i) \tag{22}$$

where f_i is the prediction frequency and $f_i \neq f_j$. Table 1 shows the values of the frequency scaling coefficients a_0 and a_1 for $f_i = 13.0$ and 31.6 GHz. The root-mean-square (rms) error increases with frequency, the correlation coefficients always being higher than 0.9. Note that in order to estimate the total path attenuation at 49.5 GHz, a quadratic best fit would give a slightly better rms error equal to 6.114 and 3.428 dB using radiometric channels at 13.0 and 31.6 GHz, respectively.

4.2. Using Radiometric and Meteorological Measurements

At a given frequency, attenuations greater than 10–15 dB cannot be generally inferred from radiometric measurements at the same frequency, because of saturation effects in T_B and radiometric noise. This problem can be tackled by using radiometric channels affected by a low atmospheric extinction and by adopting a frequency scaling approach.

Table 1. Frequency Scaling Coefficients a_0 and a_1, Given in Equation (22), to Derive the Total Path Attenuation A (in Decibels), Using Total Path Attenuation for a 20° Elevation Angle

f, GHz	a_0	a_1	RMS, dB	Correlation Coefficient
		f_i = 13.0 GHz		
18.7	0.284	1.956	0.250	0.999
23.8	1.171	2.959	0.737	0.995
31.6	1.375	4.487	1.942	0.986
39.6	3.306	5.823	3.695	0.970
49.5	9.132	7.050	6.559	0.938
		f_i = 31.6 GHz		
13.0	−0.218	0.216	0.426	0.986
18.7	−0.193	0.427	0.594	0.993
23.8	0.377	0.561	0.549	0.997
39.6	1.291	1.315	1.239	0.997
49.5	6.324	1.619	3.740	0.980

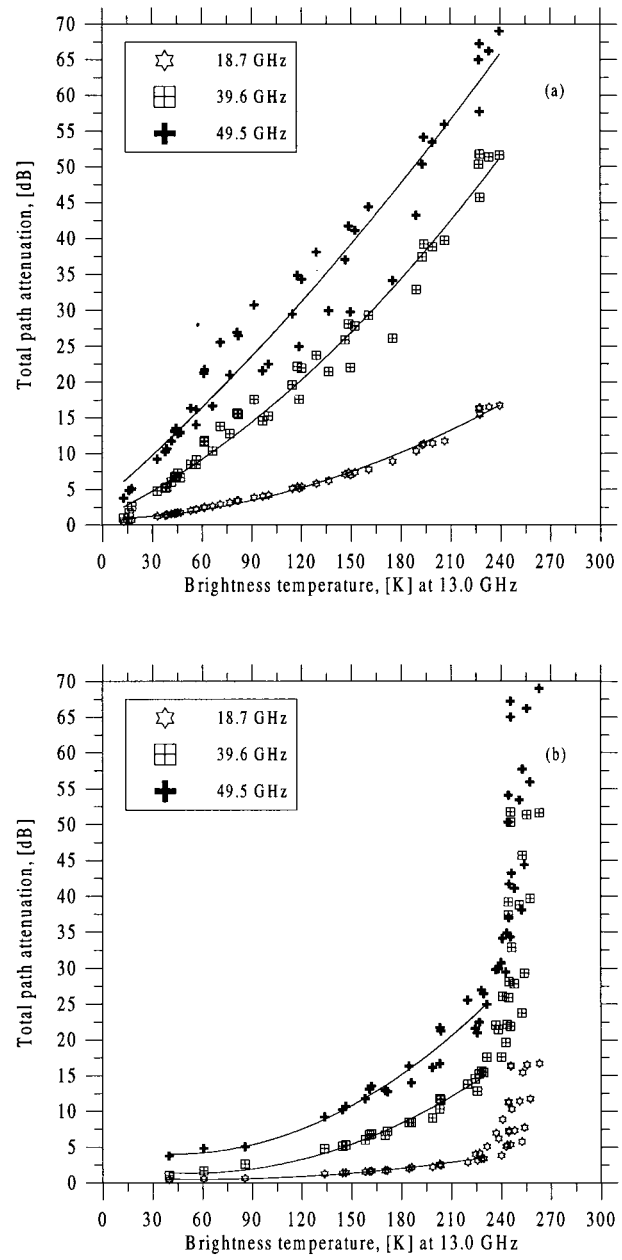

Figure 13. Total path attenuation at 18.7, 39.6, and 49.5 GHz as a function of the simulated brightness temperature at (a) 13.0 GHz and (b) 31.6 GHz, using all the simulated data set for a 20° elevation angle. Quadratic best-fittings are also shown.

Figures 13a and 13b show the total path attenuation at 18.7, 39.6, and 49.5 GHz as a function of the simulated brightness temperature at 13.0 and 31.6 GHz, respectively, using the simulated data set. We have considered also the predictor at 31.6 GHz

Table 2. Prediction Coefficients b_0, b_1, and b_2, given in Equation (23), to Derive the Total Path Attenuation A (in Decibels), Using Downwelling Brightness Temperature for a 20° Elevation Angle

f, GHz	b_0	b_1	b_2	RMS, dB	Correlation Coefficient
			f_i = 13.0 GHz		
18.7	0.7863	0.0071	0.0002	0.430	0.975
39.6	1.1361	0.1032	0.0004	3.353	0.968
49.5	3.5685	0.1911	0.0003	5.815	0.950
			f_i = 31.6 GHz		
18.7	1.8416	−0.0372	0.0002	1.682	0.632
39.6	4.0355	−0.0833	0.0006	2.309	0.853
49.5	6.6330	−0.0838	0.0007	2.144	0.906

because unlike the 13.0-GHz channel, it is available at most ground-based radiometric stations.

From the results shown in the preceding figures, an estimation of the total path attenuation A (in decibels) can be derived directly from ground-based brightness temperatures T_B (in kelvins) using a quadratic relationship, that is,

$$A(f_j) = b_0 + b_1 T_B(f_i) + b_2 T_B^2(f_i) \tag{23}$$

where f_i is equal to either 13.0 or 31.6 GHz, while the total path attenuation is evaluated at one of the operating Italsat beacons at 18.7, 39.6, and 49.5 GHz. Table 2 shows the values of the prediction coefficients b_0, b_1, and b_2 for f_i = 13.0 and 31.6 GHz. Note that because of the saturation effects noted in Figure 13b, the regression coefficients for f_i = 31.6 GHz are valid only for $T_B \leq 230$ K.

It is also interesting to derive, from the simulated data set, statistical relationships to estimate the total path attenuation (in decibels) from the surface rain rate R (in mm/h) by means of a usual power law:

$$A(f_j) = \alpha R^{\beta} \tag{24}$$

where α and β have been calculated by using a regression technique. Table 3 shows the values of the prediction coefficients α and β for frequencies f_j ranging from 13.0 to 50.2 GHz. Note that in Table 3 the β coefficients are smaller than the ones proposed in the literature [*International Telecommunication Union*, 1990; *Maggiori*, 1981], which are given for specific attenuation, i.e., dB/km. The noted discrepancy mainly depends on the rain cell finite geometry, which yields optical thickness values smaller than those of an equivalent rain slab, as pointed out in Figure 11. Moreover, in our case we also included gaseous and cloud attenuation, while the cited references only consider rainfall contribution.

5. Conclusions

An iterative solution of a 3-D RTE has been described and applied to simulate radiometric and attenuation observations of cylindrical rain cells at frequencies beyond 10 GHz. The complete cloud model takes into account the presence of liquid and ice hydrometeors, so that it produces results representative of convective storms observed from ground-based radiometers along Earth-satellite paths. The impact of different drop size distributions and variable rain cell radii has been also evaluated. Simulation results have shown some typical effects due to the 3-D volume properties, such as an absolute maximum of observed brightness temperatures with elevation scanning in case of intense precipitation and a relative sensitivity to azimuthal variations in antenna pointing.

Comparisons between 3-D rain cell and 1-D rain slab results have shown significant differences in simulated brightness temperature and path attenuation values. An equivalent slab height has been introduced in order to reduce these discrepancies for rainfall albedo less than 0.2, an assumption which is basically valid at 13.0 GHz for any rain rate and at 31.6 GHz for rain rates less than 20 mm/h.

On the basis of the data set of simulated observations of cylindrically shaped convective clouds, frequency scaling coefficients for estimating the total path attenuation have been derived for Italsat channel frequencies supposing an observation outside the rain cell. Moreover, statistical prediction of the total path attenuation has been also proposed using either surface rain rate or brightness temperatures measured by ground-based microwave radiometers. Dif-

Table 3. Prediction Coefficients α and β, Given in Equation (24), to Derive the Total Path Attenuation A (in decibels) for a 20° Elevation Angle, Using Surface Rainfall Rate (in mm/h)

f, GHz	α	β	RMS, dB	Correlation Coefficient
13.0	0.2072	0.8235	0.221	0.961
18.7	2.2156	0.2955	0.590	0.810
23.8	4.2120	0.2584	0.523	0.805
31.6	5.0990	0.3166	0.629	0.811
39.6	7.7919	0.2964	0.613	0.799
49.5	14.970	0.2216	0.501	0.773

ferences with analogous relationships reported in the literature have been mainly attributed to the impact of 3-D geometry on the simulation results, an aspect not generally taken into account in the considered references. Future work will focus on comparing attenuation predictions, based on the proposed model, with experimental measurements of colocated multichannel radiometers and satellite beacon receivers.

Acknowledgments. This research has been partially supported by Ministero dell'Università e Ricerca Scientifica e Tecnologica (MURST) and by Agenzia Spaziale Italiana (ASI). We thank the reviewers for their careful reading of the paper and for their useful suggestions.

References

Basili, P., P. Ciotti, G. d'Auria, F. S. Marzano, and N. Pierdicca, Microwave radiometry characterization of precipitating clouds, in *Microwave Radiometry of the Environment*, edited by D. Solimini, pp. 229–237, VSP Press, Utrecht, Netherlands, 1995.

Brussaard, G., Radiometry: A useful prediction tool?, *Rep. SP-1071*, Eur. Space Agency, Nordwijk, Netherlands, 1985.

Capsoni, C., F. Fedi, and A. Paraboni, A comprehensive meteorologically oriented methodology for the prediction of wave propagation parameters in telecommunication applications beyond 10 GHz, *Radio Sci.*, *22*, 387–393, 1987.

Crane, R. K., Comparative evaluation of several rain attenuation prediction models, *Radio Sci.*, *20*, 843–863, 1985.

De Angelis, G., A. Paraboni, C. Riva, F. Zaccarini, G. Dellagiacoma, L. Ordano, R. Polonio, M. Mauri, and A. Pawlina, Attenuation and scintillation statistics with Olympus and Italsat satellites in Italy, *Alta Freq.*, *6*, 66–69, 1994.

Fionda, E., M. J. Falls, and E. R. Westwater, Attenuation at 20.6, 31.6, and 52.85 GHz derived from emission measurements by ground-based microwave radiometer, *IEE Proc.*, *Part H*, *138*, 46–50, 1991.

Gasiewskii, A. J., Microwave radiative transfer in hydrometeors, in *Atmospheric Remote Sensing by Microwave Radiometry*, edited by M. A. Jansen, pp. 91–144, John Wiley, New York, 1993.

Houze, R. A., Structures of atmospheric precipitation systems: A global survey, *Radio Sci.*, *16*, 671–689, 1981.

International Telecommunication Union—Radiocommunication, Propagation in non-ionized media, *ITU-R Rep. 720-3*, pp. 226–245, Geneva, 1990.

Ishimaru, A., and R. L. T. Cheung, Multiple scattering effect on radiometric determination of rain attenuation at millimeter wavelengths, *Radio Sci.*, *15*, 507–516, 1980.

Kozu, T., J. Awaka, H. Fukuchi, and K. Nakamura, Rain attenuation ratios on 30/20- and 14/12-GHz satellite-to-Earth paths, *Radio Sci.*, *23*, 409–418, 1988.

Kummerow, C., and J. A. Weinman, Determining microwave brightness temperatures from precipitating horizontally finite and vertically structured clouds, *J. Geophys. Res.*, *93*, 3720–3728, 1988.

Liebe, H. J., T. Manabe, and G. A. Hufford, Millimeter-wave attenuation and delay rates due to fog/cloud conditions, *IEEE Trans. Antennas Propag.*, *37*, 1617–1623, 1989.

Maggiori, D., Computed transmission through rain in the 1–400 GHz frequency range for spherical and elliptical drops and any polarization, *Alta Freq.*, *L*, 262–273, 1981.

Mass, J., A simulation study of rain attenuation and diversity effects on satellite links, *COMSAT Tech. Rev.*, *17*, 159–188, 1987.

Misme, P., and P. Waldteufel, A model for attenuation by precipitation on a microwave Earth-space link, *Radio Sci.*, *15*, 655–665, 1980.

Mugnai, A., and E. A. Smith, Radiative transfer through a precipitating cloud at multiple microwave frequencies, I, Model description, *J. Appl. Meteorol.*, *27*, 1055–1073, 1988.

Olsen, R. L., D. V. Rogers, and D. B. Hodge, The aR^b relation in the calculation of rain attenuation, *IEEE Trans. Antennas Propag.*, *AP-26*, 318–329, 1978.

Pierdicca, N., F. S. Marzano, G. d'Auria, P. Basili, P. Ciotti, and A. Mugnai, Precipitation retrieval from spaceborne microwave radiometers based on maximum a posteriori probability estimation, *IEEE Trans. Geosci. Remote Sens.*, *34*, 831–846, 1996.

Roberti, L., J. Haferman, and C. Kummerow, Microwave radiative transfer through horizontally inhomogeneous precipitating clouds, *J. Geophys. Res.*, *99*, 16,707–16,718, 1994.

Schiavon, G., D. Solimini, and E. R. Westwater, Performance analysis of a multifrequency radiometer for predicting atmospheric propagation parameters, *Radio Sci.*, *28*, 63–76, 1993.

Slobin, S., Microwave noise temperature and attenuation of clouds: Statistics of these effects at various sites in the United States, Alaska, and Hawaii, *Radio Sci.*, *17*, 1443–1454, 1982.

Smith, E. A., and A. Mugnai, Radiative transfer through a precipitating cloud at multiple microwave frequencies, II, Results and analysis, *J. Appl. Meteorol.*, *27*, 1074–1091, 1988.

Smith, E. A., A. Mugnai, H. J. Cooper, G. J. Tripoli, and X. Xiang, Foundations for statistical-physical precipitation retrieval from passive microwave satellite measurements, I, Brightness-temperature properties of a time-dependent cloud-radiation model, *J. Appl. Meteorol.*, *31*, 506–531, 1992.

Smith, E. A., X. Xiang, A. Mugnai, and G. J. Tripoli, Design of an inversion-based precipitation profile retrieval algo-

rithm using an explicit cloud model for initial guess microphysics, *Meteorol. Atmos. Phys*., *54*, 53–78, 1994.

Stamnes, K., S. Tsay, W. Wiscombe, and K. Jayaweera, Numerically stable algorithm for discrete-ordinate-method radiative transfer in multiple scattering and emitting layered media, *Appl. Opt*., *27*, 2502–2509, 1988.

Tsang, L., J. A. Kong, and R. T. Shin, *Theory of Microwave Remote Sensing*, John Wiley, New York, 1985.

Ulaby, F. T., R. K. Moore, and A. K. Fung, *Microwave Remote Sensing: Active and Passive*, vol. I, *Fundamentals and Radiometry*, Addison-Wesley, Reading, Mass., 1982.

Watson, P. A., and Y. G. Hu, Prediction of attenuation on satellite-Earth links for systems operating with low fade margins, *IEE Proc*., *Part H*, *Microwaves Antennas Propag*., *141*, 467–472, 1992.

Westwater, E. R., J. B. Snider, and M. J. Falls, Ground-based radiometric observation of atmospheric emission and attenuation at 20.6, 31.65 and 90.0 GHz: A comparison of measurements and theory, *IEEE Trans. Antennas Propag*., *AP-38*, 1569–1580, 1990.

Wiscombe, W., Improved Mie scattering algorithms, *Appl. Opt*., *19*, 1505–1509, 1978.

Wu, R., and J. A. Weinman, Microwave radiances from precipitating clouds containing aspherical ice, combined phase, and liquid hydrometeors, *J. Geophys. Res*., *89*, 7170–7178, 1984.

P. Ciotti and F. S. Marzano, Dipartimento di Ingegneria Elettrica, Università dell'Aquila, Monteluco di Roio, 67040 L'Aquila, Italy. (marzano@ing.univaq.it; ciotti@ing.univaq.it)

E. Fionda, Fondazione Ugo Bordoni, Viale Europa, 00144, Roma, Italy. (ermanno@fub.it)

(Received April 8, 1998; revised January 25, 1999; accepted March 3, 1999.)